Cross-shore suspended sediment transport in a macro-tidal and low-sloping upper shoreface

Marc Pezerat, Xavier Bertin, Thibault Coulombier

Cross-shore suspended sediment transport in a macro-tidal and low-slopping upper shoreface

Marc Pezerat*[1], Xavier Bertin[2], and Thibault Coulombier[2]

[1]Service Hydrographique et Océanographique de la Marine (SHOM), Brest, France
[2]UMR 7266 LIENSs, CNRS - La Rochelle Université, La Rochelle, France

Abstract

The driving mechanisms of sediment transport across the upper shoreface have yet been poorly examined because of the scarcity of field measurements beyond the inter-tidal area, which is mainly due to instrumentation difficulties. Here, we investigate the cross-shore suspended sediment transport from synchronized timeseries of bottom pressure, current velocity and suspended sediment concentration measured by 13 m water depth, in a macro-tidal and low-slopping shoreface, under storm waves and fair weather conditions. Depending on the tidal phase and the incoming wave height, the measuring structure was alternatively located in the shoaling zone and in the outer surfzone. The analysis of field observations first revealed that steady currents dominate suspended transport, with a notable contribution of the wave driven return current under storm wave conditions. Cross-spectral analysis further indicates that short waves globally induce an offshore-directed transport under energetic conditions associated with a crest-to-trough phase lag effect. The contribution of infragravity (IG) waves, which reaches as much as 20% of the total transport, shows contrasting directions depending on whether IG waves are bound to the short wave groups or propagate as free waves.

Keywords

Suspended sediment transport, shoreface, undertow, short waves, phase lag, IG waves

1 Introduction

At seasonal to decadal timescales, the shoreface transitionning between the surf zone and the shelf plays a fundamental role in the morphological evolution of adjacent shorelines (Hamon-Kerivel et al., 2020). In coastal regions characterized by large tidal ranges and gently sloping shoreface, this transition region can shift by several kilometers in the cross-shore direction, depending on the tidal phase and the incoming wave height (e.g. see Pezerat et al., 2022).

It is ackowledged that sediment transport generally takes place as both bedload and suspended load, but fine sandy sediments are more likely transported in suspension across wave-exposed nearshore area (e.g. Jaffe et al., 1985; Osborne and Greenwood, 1992; Russell, 1993). Several studies further showed that suspended sediment transport on beaches is associated with both oscillatory wave motions and steady currents, i.e. time-averaged over several wave periods (e.g. Osborne and

*Corresponding author: marc.pezerat@shom.fr

Greenwood, 1992; Russell, 1993; Ruessink et al., 1998). In situ observations support the fact that the oscillatory transport within the gravity (G) band - in frequency (f) space - associated with short waves (0.04 Hz $\lesssim f \lesssim$ 0.4 Hz) is mainly onshore-directed and dominates the suspended load motion under moderate wave energy conditions (Osborne and Greenwood, 1992; Russell, 1993). Based on laboratory experiments, several studies further related the transport at short wave frequencies under sheet flow regime to the wave shape that is determined by a certain degree of skewness and asymmetry (e.g. Dibajnia and Watanabe, 1992; Dohmen-Janssen et al., 2002; Hsu and Hanes, 2004; Grasso et al., 2011). Skewed waves are characterized by stronger velocities in the direction of propagation under their crests, hence (presumably) mobilizing a larger amount of sediment than under their troughs, below which the velocity is oriented in the opposite direction. While Hsu and Hanes (2004) found that the transport is oriented in the direction of wave propagation under skewed waves, Dohmen-Janssen et al. (2002) and Grasso et al. (2011) actually observed that the orientation of the transport depends on the phase lag between the wave passing and the re-suspension event. For highly skewed waves, the peak of suspended sediment concentration could be slightly shifted in time to be found concomitant with the wave's trough, which thus results in a transport offshore-directed (crest-to-trough phase lag effect). Within the surf zone, waves become more asymmetric, resulting in a skewed acceleration over the wave period as the acceleration is stronger under the front face than under the rear face of the wave (see Elgar et al., 2001, their Fig.1). Several studies reported that sediment resuspension is more likely correlated with orbital acceleration (e.g. Hanes and Huntley, 1986; Jaffe and Rubin, 1996), such that for asymmetric waves, a trough-to-crest phase lag is induced between the resuspension event and the wave passing, resulting in a transport onshore-directed. Infragravity (IG) waves (0.001 Hz $\lesssim f \lesssim$ 0.04 Hz) have also a direct bearing on suspended sediment transport, although observations result in contrasting direction and relative importance of the associated transport (see the pioneering studies from Abdelrahman and Thornton, 1987; Beach and Sternberg, 1988; Roelvink and Stive, 1989; Osborne and Greenwood, 1992; Russell, 1993, among many others). de Bakker et al. (2016) proposed a conceptual model relying on the local ratio of IG wave height to short wave height to infer the direction of the transport and its relative importance based on observations collected either on moderately or gently sloping beach to account for the different IG waves propagation regime, depending on whether IG waves are bound to the short wave groups or propagate as free waves. Finally, the wave-driven return current (the so-called undertow) was found to be the main mechanism that induces an offshore directed transport within the surf zone (e.g. Russell, 1993; Ruessink et al., 1998).

The driving mechanisms of the cross-shore sediment transport beyond the inner surf zone are still poorly understood because of the scarcity of field measurements in relatively deeper water, which is mainly due to instrumentation difficulties, especially under storm conditions. In this context, the present study aims to investigate the relative contributions to cross-shore suspended sediment transport over the macro-tidal and low sloping upper shoreface in front of a beach made of fine sands, based on in situ measurements at a 12.8 m-depth location. The dataset covers storm events as well as fair weather conditions, thus encompassing a variety of forcing regimes.

2 Methods

2.1 Study area

The study area is located in front of Saint-Trojan beach, a 8 km-long sandspit along the South-Western coast of the Oléron Island in the central part of the French Atlantic coast (Fig. 1a). This stretch of coast spans in a North-West to South-East direction forming an angle of approximately 5° from the true North at the median latitude. This area is characterized by a very gently sloping shoreface (the isobath 20 m being found 10 km offshore, see Fig. 1b) and a non-barred dissipative beach composed of fine sandy sediments with a median grain size of the order of 0.2 mm (Bertin et al., 2008). In this region, tides are semi-diurnal and range from 1.5 to 5.5 m, which corresponds to a macro-tidal regime. Yearly mean wave conditions along the 30 m isobath are characterized by a significant wave height of 1.6 m, a mean wave period of 5.9 s and a direction of 285° from the true North (Dodet et al., 2019), but the offshore significant wave height can exceed 10 m with peak periods over 20 s (Bertin et al., 2015).

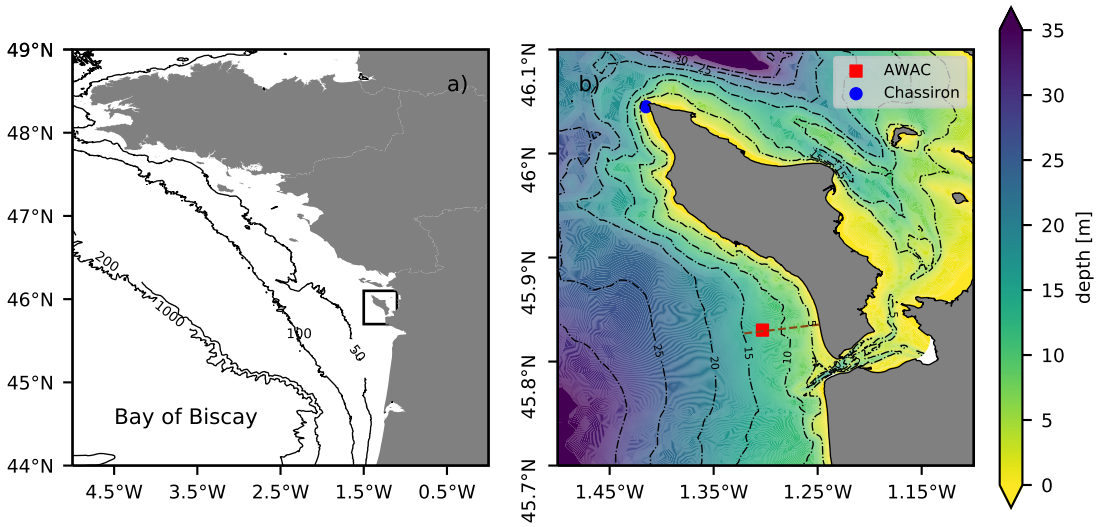

Figure 1: **a)** Location of the study area in the bay of Biscay. **b)** Bathymetric map of the study area with isobaths reduced to the Mean Sea Level (MSL) displayed every 5 m (black dash-dotted lines), sensors location and position of the Chassiron meteorological station while the dashed line symbolizes the cross-shore direction.

2.2 Field campaign and data processing

This study builds on the field campaign carried out between January and February 2021 already presented by Pezerat et al. (2022). The measurements from a high resolution (1 MHz) Acoustic Wave and Current Profiler (AWAC) deployed by 12.8 m-depth below MSL are here combined with measurements from an Optical Backscatter Sensor (OBS) that was plugged to the AWAC and deported 0.5 m above its head. The OBS signal intensity was converted into Suspended Sediment Concentration (SSC) after a calibration in the laboratory, using sediment samples collected at the location of the instruments. The measurements alternated a "current cycle" and a "wave cycle" each hour. During the "current cycle", 10-min averaged velocity profile measurements were col-

lected along the vertical axis, while during the "wave cycle", velocity measurements within a fixed cell located 4.5 m above sensor's head, bottom pressure measurements and SSC measurements were performed at 2 Hz during 20 minutes. Pressure measurements were first corrected for sea level atmospheric pressure using data collected at the nearby meteorological station of Chassiron (Fig. 1b), detrended and converted into a sea surface elevation signal assuming a hydrostatic pressure. Pressure attenuation with depth due to non-hydrostatic effects was then corrected using the Transfer Function Method based on the linear theory (TFM, e.g. see Bishop and Donelan, 1987) to compute the short waves free surface elevation signal (η_L). This method requires an upper cutoff frequency (f_c, here set to 0.2 Hz) so as to remove high frequency noise that is amplified by the TFM correction and to prevent the over-amplification of high-frequency energy levels due to non-linear interactions in intermediate and shallow-water depths (Mouragues et al., 2019). Finally the sea surface elevation density spectra $E(f)$ were computed by means of a fast Fourier Transform on 5 Hanning-windowed segments with a 50% overlap which allows an *ad hoc* compromise between statistical stability (10 degrees of freedom) and frequency resolution (4.2 mHz) required to investigate the contributions to the elevation signal from both the G and the IG bands. The spectral significant wave height (H_{m0}) and the continuous peak period (T_{pc}) were computed using the $p-th$ moments of the spectra:

$$m_p = \int_{f_{min}}^{f_{max}} f^p E(f) df \tag{1}$$

such that:

$$H_{m0} = 4\sqrt{m_0} \tag{2}$$

and,

$$T_{pc} = \frac{m_{-2} m_1}{m_0^2} \tag{3}$$

where f_{min} was set to 0.001 Hz for the IG band and f_{max} was set to $f_c = 0.2$ Hz for the G band, while both spectral domains were separated based on the separation frequency $f_{min,G}$ defined as half the peak frequency (Hamm and Peronnard, 1997; Bertin et al., 2020).

During the studied period, the waves globally reached the study area from a Westward direction, almost normally incident to the shoreline, suggesting a prevailing contribution of the cross-shore transport. The data from the "wave cycle" were thus used to compute the time-averaged sediment transport rate in suspension along the cross-shore direction. It is worth pointing out that velocity and SSC measurements were not vertically co-located, such that the quantitative estimate of the sediment fluxes is presumably biased. It is nonetheless assumed that both measurements show consistent patterns allowing to identify the relative contributions of the different forcing processes involved. This strong assumption is found justified for three reasons: (i) considering the forcing conditions, the transport of fine sandy sediment likely takes place as suspended load (see Appendix C), (ii) the decrease of short wave orbital velocities between the wave cell and the OBS roughly estimated by means of the linear wave theory, is rather moderate, of the order of few percents (see Appendix B) and (iii) the steady current keep the same orientation along the vertical at this scale (e.g., see Pezerat et al., 2022). Following the seminal approach of Jaffe et al. (1985), instantaneous SSC (c) and cross-shore velocity (u) are decomposed into a mean ($\bar{\cdot}$) and an oscillating component

$(\tilde{\cdot})$ such that the time-averaged sediment flux reads:

$$q_{tot} = \overline{uc} = \overbrace{\overline{u}\overline{c}}^{q_{mean}} + \overbrace{\overline{\tilde{u}\tilde{c}}}^{q_{osc}} \tag{4}$$

where q_{mean} corresponds to the transport forced by the mean current, that integrates tidal current and the wave-driven mean current, and q_{osc}, also referred to as the flux coupling, measures the correlation between the fluctuations of velocity and concentration. This term can be readily estimated from the co-spectrum between $\tilde{u}$ and $\tilde{c}$, which is the real part ($\Re\{\cdot\}$) of the cross-spectrum between both signals ($S_{\tilde{u}\tilde{c}}$):

$$q_{osc} = \int_f \Re\{S_{\tilde{u}\tilde{c}}\}df = \overbrace{\int_{f_{min,IG}}^{f_{min,G}} \Re\{S_{\tilde{u}\tilde{c}}\}df}^{q_{osc}^{IG}} + \overbrace{\int_{f_{min,G}}^{f_{max}} \Re\{S_{\tilde{u}\tilde{c}}\}df}^{q_{osc}^{G}} \tag{5}$$

where f_{max} was here set to 0.4 Hz as measurements were directly considered. For each 20 min-long burst, raw signals were first detrended to compute the oscillating components of both signals. The cross-spectrum was then computed from the product of the conjugate of the Fourier transform of $\tilde{u}$ with the Fourier transform of $\tilde{c}$ using again 5 Hanning-windowed segments with a 50% overlap. Finaly, the relative absolute contributions of each term to the time-averaged sediment flux is given by:

$$R_X = \frac{|X|}{|q_{mean}| + |q_{osc}^{IG}| + |q_{osc}^{G}|} \tag{6}$$

where X represents either q_{mean}, q_{osc}^{G} or q_{osc}^{IG}.

3 Results

The local time-averaged sediment flux is alternatively of very low intensity (e.g. between the 05/02 and 08/02), positive (i.e. onshore-directed) or negative (i.e. offshore-directed). Overall, the transport forced by the mean current (q_{mean}) dominates, with a relative contribution averaged over the entire time period reaching 88%. One can observe for instance the strong tidal modulation of q during spring tides between the 10/02 and the 20/02, with a transport alternatively onshore- or offshore-directed depending on the tidal phase (Fig. 2a,d). During the first spring tides, concomitant with the main storm episode (between the 28/01 and the 05/02, see the grey shaded area in Fig. 2), Pezerat et al. (2022) showed that the cross-shore mean current is mostly offshore-directed associated with the prevailing contribution of the wave driven return current generating a jet like circulation with a local current intensity reaching as much as 0.25 m/s at the peak of the storm. As a result, the local time-averaged cross-shore sediment transport is mostly offshore-directed, reaching up to -7.3 kg/m^2/s, such that flood currents are not intense-enough to reverse the orientation of the transport (Fig. 2d). For some bursts, the flux coupling contributes predominantly to the sediment transport, especially under energetic conditions (Fig. 2e). The results show a prevailling contribution of the flux coupling in the G band as compared to the IG band, associated with a low local ratio ($\simeq 10\%$) of IG wave height to short wave height (Fig 2b,e), which was found to be a pertinent proxy for the contribution of IG waves to sediment transport (de Bakker et al., 2016). Focusing on the energetic episode, the co-spectra reveal contrasting dynamics with direction reversals within both the IG and the G bands (Fig 3a). It is worth pointing out that the order of

magnitude for the time-averaged sediment flux is fairly consistent with the results of the literature ($q \simeq 5\,\mathrm{kg/m^2/s}$ Russell, 1993; Osborne and Greenwood, 1992; de Bakker et al., 2016), although previous studies typically relied on in situ measurements collected in the inter-tidal area.

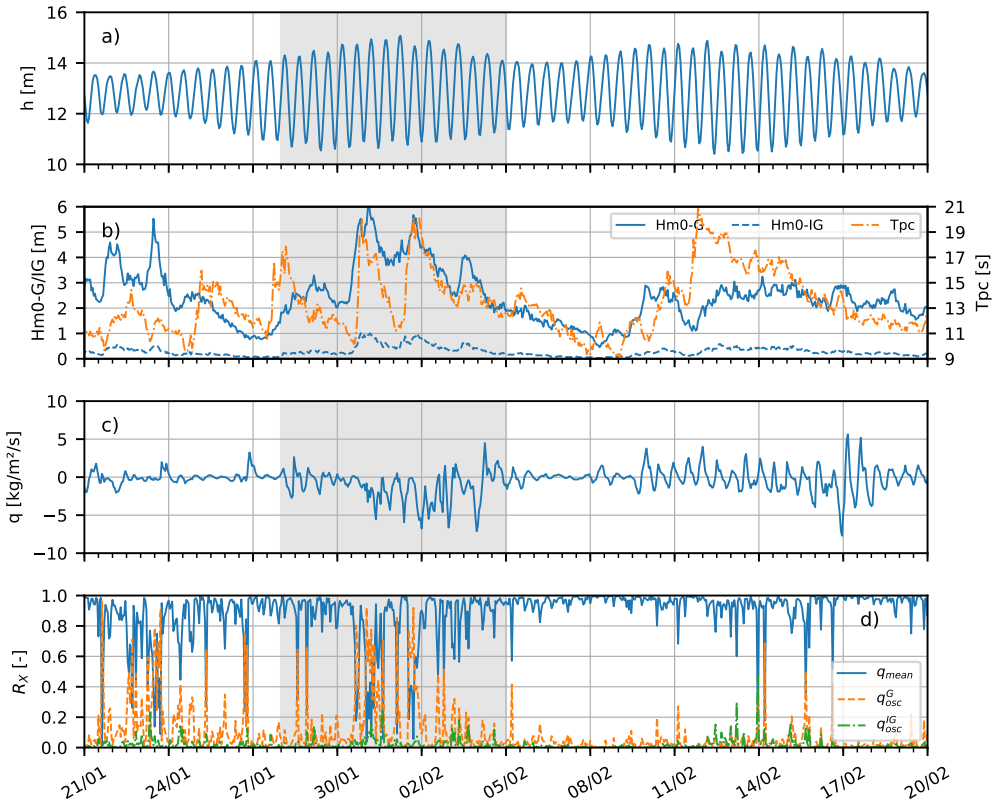

Figure 2: **a)** Burst-averaged water depth. **b)** Short waves and IG waves significant height and continuous peak period of short waves. **c)** Net time-averaged cross-shore sediment transport rate. **d)** Relative absolute contributions of each component of the transport. The grey shaded area in each panel covers the storm event studied by Pezerat et al. (2022).

4 Discussion

4.1 Suspended sediment transport by short waves

The contribution of short waves is further investigated regarding the phase-lag between $\tilde{u}$ and $\tilde{c}$ within the G band, which reads:

$$\Phi^G = \int_{f_{min,G}}^{f_{max}} \arctan\left(\frac{\Im\{S_{\tilde{u}\tilde{c}}\}}{\Re\{S_{\tilde{u}\tilde{c}}\}}\right) df \tag{7}$$

where $\Im\{\cdot\}$ designates the Imaginary part. The phase-lag is examined in relation to the development of the short wave skewness and asymmetry, respectively estimated through the two following

parameters (e.g. Elgar and Guza, 1985):

$$Sk = \frac{\overline{\tilde{u}_G^3}}{\overline{\tilde{u}^2}^{3/2}} \tag{8}$$

and,

$$As = \frac{\overline{\mathcal{H}\{\tilde{u}_G\}^3}}{\overline{\tilde{u}_G^2}^{3/2}} \tag{9}$$

where $\tilde{u}_G$ is obtained by correcting $\tilde{u}$ from the low-pass filtered signal with a cutoff frequency set to $f_{min,G}$, while $\mathcal{H}\{\cdot\}$ designates the Hilbert's transform. The values of Sk are typically between 0 and 1 (the higher the value of Sk, the more the waves are skewed), whereas the values of As are usualy negative between 0 and -1.5 (the lower the value of As, the more the waves are asymmetric). While the asymmetry remains relatively weak, the skewness is particularly developed at the storm peaks (e.g. around the 31/01 and 02/02, see Fig. 3b). The results tend to show that the transport is mostly offshore-directed when Φ^G is negative, concomitantly with high Sk values (Fig. 3a,b), which is consistent with the crest-to-trough phase lag effect described by Grasso et al. (2011) from their laboratory experiments. This phase lag is readily observed by comparing the timeseries of $\tilde{u}$ and c for a given burst (Fig. 3c,d).

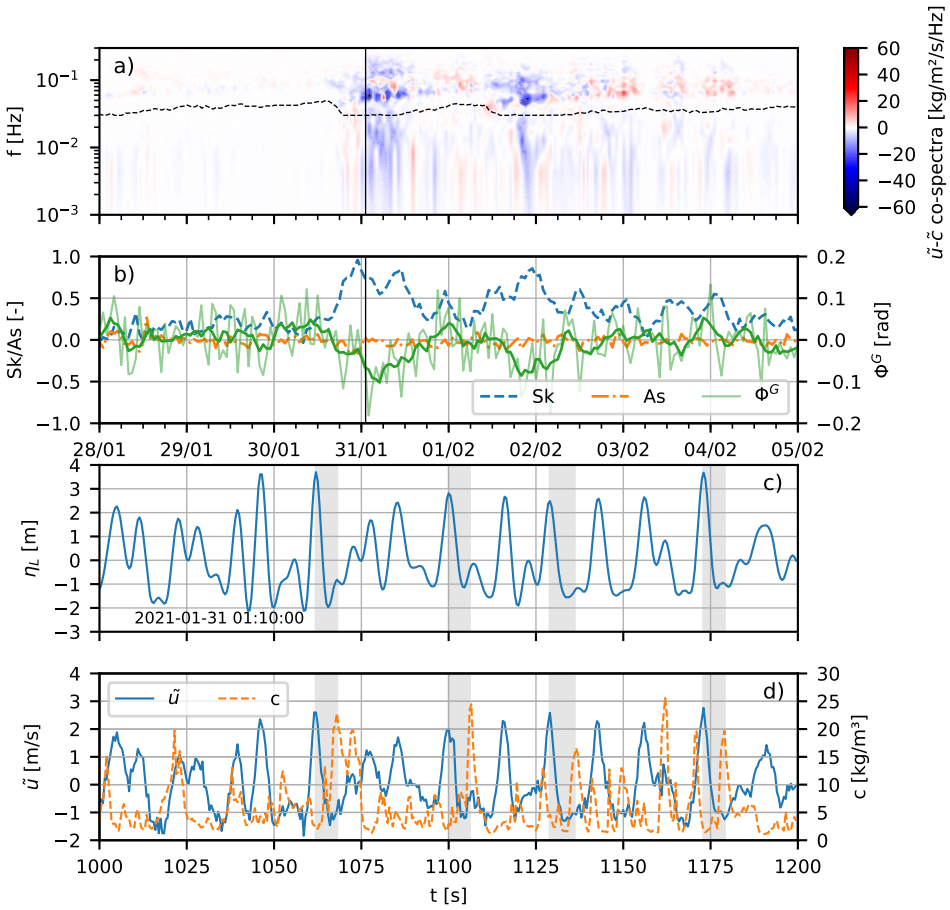

Figure 3: **a)** $\tilde{u}$-$\tilde{c}$ co-spectra and separation frequency between the IG and G bands ($f_{min,G}$, see the black dashed line). **b)** Short waves skewness (Sk) and asymmetry (As) and phase lag between $\tilde{u}$ and $\tilde{c}$ at short wave frequencies (raw signal in light green and 6 h-running-averaged signal in dark green). **c)** Burst sample of the short waves free surface elevation signal (see the black vertical line in panels **a** and **b** for the burst considered). **d)** Burst sample of $\tilde{u}$ and c. The grey-shaded area highlight the phase-lag between the maxima of short waves orbital velocity and the peak of SSC.

4.2 Suspended sediment transport by IG waves

Although the contribution of the flux coupling within the IG band is overall of second order, its relative contribution reaches as much as 20% at the peak of the storm (e.g. the 31/01, just before 6 h, see Fig. 2e). The direction of the cross-shore transport that occurs within the IG band is further analysed. Following de Bakker et al. (2016), the correlation between the incoming IG waves and the short wave energy envelope is quantified to estimate whether the IG waves are bound to the short wave group or propagate as free waves. The low-pass filtered reconstructed free surface elevation (η_{IG}) is first partitioned into incoming (η^+_{IG}) and outgoing (η^-_{IG}) IG wave signals using the approach of Van Dongeren and Svendsen (1997) (their Eq. 4.30):

$$\begin{aligned} \eta^+_{IG} &= \frac{\sqrt{gh}\eta_{IG}+Q}{c_g+\sqrt{gh}} \\ \eta^-_{IG} &= \frac{c_g\eta_{IG}-Q}{c_g+\sqrt{gh}} \end{aligned} \tag{10}$$

with:

$$Q = \tilde{u}_{IG}(h + \eta_{IG}) \tag{11}$$

where $\tilde{u}_{IG}$ is obtained by low-pass filtering $\tilde{u}$ with a cutoff frequency set to $f_{min,G}$. These equations are modified versions of those given by Guza et al. (1985), extending their approach to the shoreface by assuming that incoming waves travel at the speed of short wave groups and outgoing waves propagate as free waves. The reflection coefficient ($\mathcal{R}^2$) is thus defined as the ratio between the incoming and the outgoing energy. The envelope of the short wave elevation signal (A) is computed following the procedure described by List (1991) and the Groupiness Factor (GF) is finally introduced to quantify the modulation of the amplitude of the elevation signal corresponding to the presence of groups, such as (List, 1991):

$$\mathrm{GF} = \frac{\sqrt{2}\sigma_A}{\overline{A}} \tag{12}$$

where σ_A is the standard deviation of A. A strong tidal modulation of the reflection coefficient is observed under moderate wave energy conditions, with $\mathcal{R}^2 \lesssim 0.5$ at low tides and $\mathcal{R}^2 \gtrsim 1$ at high tides (Fig. 4a,b), suggesting a total reflection at the shoreline. The values of $\mathcal{R}^2$ above unity would indicate an increase of incoming IG waves energy between the sensor's location and the shoreline. Interestingly, the values of $\mathcal{R}^2$ drop and the tidal modulation weakens under energetic conditions (see Fig. 4b between the 30/01 and the 03/02). These results are consistent with those observed by Bertin et al. (2020) during a field campaign carried out in February 2017 under similar hydrodynamic conditions. The increase in $\mathcal{R}^2$ at high tide would be explained by a steeper slope of the beach upper part, while lower values of $\mathcal{R}^2$ would be associated with the dissipation of IG waves between the sensor and the shoreline. Bertin et al. (2020) shows indeed that, across this wide area within which breaking is active, a large amount of IG wave energy could be transferred towards higher frequency through non-linear triad interactions, which ultimately lead to IG wave breaking in shallow depth. The results further show a negative correlation between A and the incoming IG waves elevation signal associated with relatively high values of the GF (GF$\simeq 0.6$), which suggests a bound wave pattern for the incoming IG waves (Fig. 4c). The strong re-suspension by short waves at the scale of a group thus coincides with the trough of the bound IG wave associated with an offshore-directed current (Fig. 5a,c,e). This bound wave mechanism, as conceptualised by Abdelrahman and Thornton (1987) - see also Roelvink and Stive (1989) - and already reported by few studies (e.g. Osborne and Greenwood, 1992; de Bakker et al., 2016), could explain the offshore-directed transport within the IG band that is globally observed. Yet, the negative correlation occasionally decreases along with the GF (the most notable example being observed around the 30/01, midnight, see Fig. 4c), which could be interpreted as the release of bound IG waves as the highest short waves break. As the released IG waves propagate a bit faster than the weakly dispersive short waves, the crest of the IG waves would be in phase with the partially remaining groups (Fig. 5b,d,e), which would result in inverting the former mechanism.

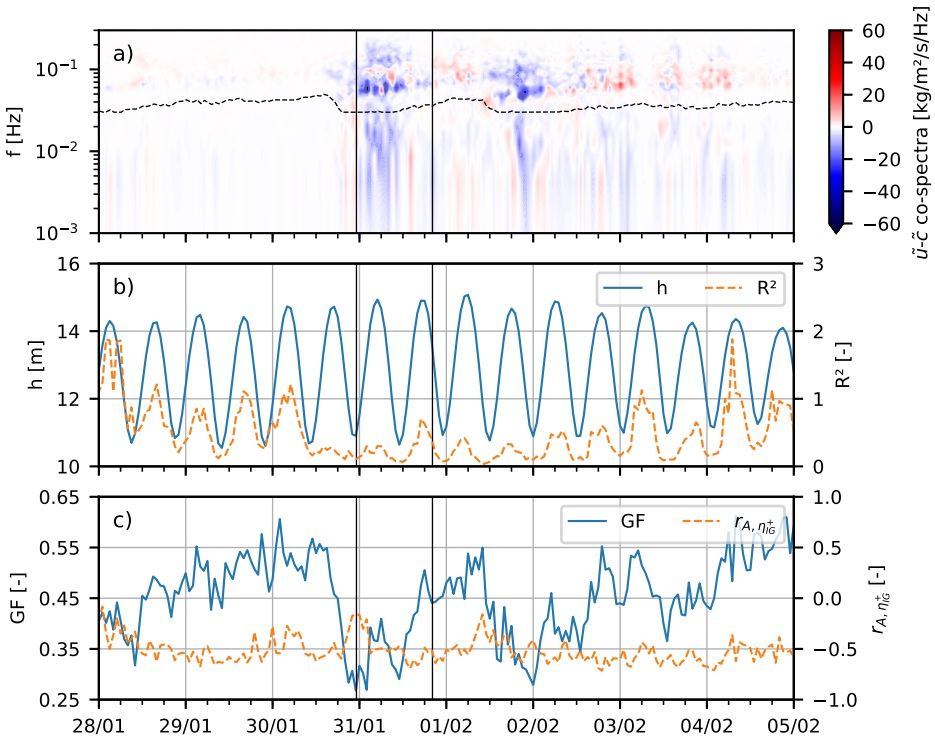

Figure 4: **a)** $\tilde{u}$-$\tilde{c}$ co-spectra and separation frequency between the IG and G bands ($f_{min,G}$, see the black dashed line). **b)** Burst-averaged water depth and squared reflection coefficient. **c)** Groupiness Factor and Pearson correlation coefficient with a confidence level of 95% between the envelope of short waves elevation signal and the incoming IG waves elevation signal.

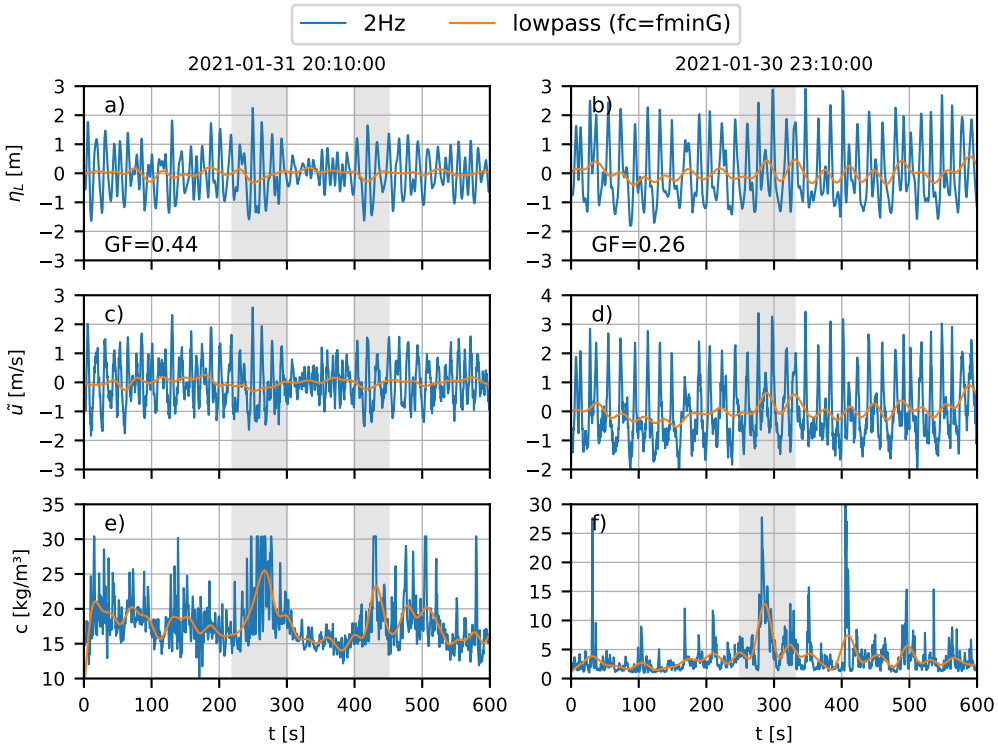

Figure 5: **a)** and **b)** Burst samples of the free surface elevation and associated IG waves free surface elevation for two bursts (see the vertical black lines in Fig. 4). **c)** and **d)** Burst samples of the oscillating component of the cross-shore velocity and associated IG waves signal. **e)** and **f)** Burst samples of SSC signal and associated signal within the IG band. The panels on the left illustrate the bound wave mechanism, whereas those on the right are representative of the transport mechanism with released incoming IG waves (see in particular the grey shaded area).

5 Conclusion

This study first shows that steady currents dominate suspended sediment transport within the upper shoreface. While tidal currents modulate the orientation of the transport under fair weather conditions, the wave driven return current is shown to force an offshore-directed sediment transport at the storm peak at the measurement location, as far as 4 km from the shoreline. Cross-spectral analysis of the oscillating transport further shows the key contribution of short wave motions especially under energetic conditions, which globally induce an offshore directed transport resulting from a crest-to-trough phase lag effect. Finally the relatively weak contribution of IG waves to suspended transport appears correctly described by the conceptual model proposed by de Bakker et al. (2016) with a transport mostly offshore directed, associated with incoming IG waves bound to the wave groups. Although based on measurements vertically not co-located, from a single location, these results highlight the processes governing the cross-shore sediment transport beyond the inner surf zone, and further advocate for a comprehensive description of the wave-driven dynamics all across the nearshore area. It thus appears crucial to repeat similar field campaigns, extending measurement locations across the shoreface and the surf zone in contrasted environment to further investigate the influence of the local bottom slope or the granulometry. Finally, these results also

question the morphodynamic modelling of nearshore areas (including the shoreface and the surf zone) when using phase-averaged wave model where IG waves are not represented and phase lag effects have to be parameterized.

Acknowledgments

Marc Pezerat was supported by a PhD fellowship from CDA La Rochelle and from the FEDER project DURALIT at the time of the field campaign, and acknowledges the EPA SHOM for presently supporting his research effort. The authors appreciate the administrative support of the DDTM to carry out long term deployment of sensors. The data were also acquired in the scope of the National Observation System DYNALIT (https://www.dynalit.fr), part of the research infrastructure ILICO. Lastly, the authors wish to thank Kévin Martins for his precious advice on cross-spectral analysis, and two anonymous reviewers for their constructive comments and suggestions.

A OBS calibration

The calibration of the OBS followed the protocol detailled in Coulombier et al. (2012). Five series of measurements were here carried out in a 70 L tank in which the sediment collected at the study site was progressively added and maintained in suspension using a stirrer and a pump. Prior to each addition of sediment, a 500 mL sample was collected to measure the concentration corresponding to the $n-th$ series of measurements after filtration and drying of the sediment contained in the sample. Several measurements were performed after addition of sediment so as to control that the system reached a steady state. The final OBS measurements of each series were then fitted to the concentration measured using a simple linear regression with a good agreement ($r^2 = 0.95$, see Figure 6), such that the fitted model could be applied to the OBS measurements collected during the field campaign.

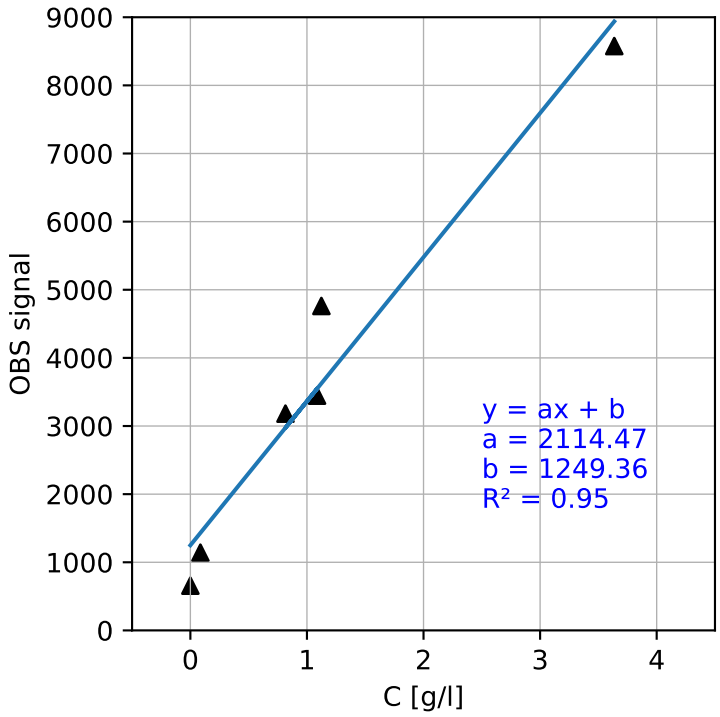

Figure 6: Linear regression resulting from the calibration procedure of the OBS sensor.

B Vertical decrease of short wave orbital velocities

The vertical decrease of short wave orbital velocities can be estimated from the depth-varying expression of orbital velocities (u_{orb}, in m/s) based on the linear wave theory:

$$u_{orb}(z) = \sigma a \frac{\cosh\left(k(z+d)\right)}{\sinh\left(kh\right)} \tag{B.1}$$

where σ is the relative pulsation (in rad/s), a is the wave amplitude (in m), k is the wavenumber (in m^{-1}) given by the dispersion relation reading $\sigma^2 = gk\tanh(kh)$, with $g = 9.81\,\mathrm{m/s^2}$, the gravitational acceleration, and z is the vertical coordinates ranging from $-d$ at the bottom to $\overline{\eta_h}$ at the free surface, such that the local mean water-depth reads $h = d + \overline{\eta_h}$. Considering a relative pulsation based on the continuous peak period representative of the sea-state (i.e. $\sigma = 2\pi/T_{pc}$), the relative decrease of short wave orbital velocities from the wave cell to the OBS vertical locations thus reads:

$$\chi_{u_{orb}} = \frac{u_{orb}(z=z_{wc}) - u_{orb}(z=z_{OBS})}{u_{orb}(z=z_{wc})} = 1 - \frac{\cosh\left(k(z_{OBS}+d)\right)}{\cosh\left(k(z_{wc}+d)\right)} \tag{B.2}$$

The result of the computation carried out over the entire studied period is presented Figure 7.

C Prevailing transport regime for fine sands

The dominance of suspended load over bedload transport usually occurs when the skin friction velocity exceeds the sediment settling velocity (Soulsby, 1997). As such, the maximum skin friction velocity under combined waves and currents (u^*_{max}, in m/s) is compared with the settling velocity

(Ws, in m/s) considering a grain size $D = 200\,\mu$m representative of the fine sand fraction of the sediment (see Figure 7). The mean (τ_m) and maximum (τ_{max}) values of the skin friction bed shear stress over a wave cycle (in Pa) were first computed by means of the following formula (Soulsby, 1997, Eq. 69 and 70):

$$\begin{aligned} \tau_m &= \tau_c \left(1 + 1.2 \left(\frac{\tau_w}{\tau_c + \tau_w}\right)^{3.2}\right) \\ \tau_{max} &= \sqrt{\left(\tau_m + \tau_w \cos\phi\right)^2 + \left(\tau_w \sin\phi\right)^2} \end{aligned} \tag{C.1}$$

where τ_w is the wave-only peak bed shear-stress, τ_c is the current-only bed shear stress and ϕ is the angle between current direction and mean wave direction, which was readily estimated through the cross-spectral analysis of orbital velocities, while classical expressions were used for τ_w and τ_c with a bed roughness length (z_0) set to $D/12$ (see Example 5.1 of Soulsby, 1997):

$$\tau_c = \rho C_d \overline{u}^2 \tag{C.2}$$

$$\tau_w = \frac{1}{2} \rho f_w U_{orb} \tag{C.3}$$

with C_d, the drag coefficient and f_w, the wave friction factor, that respectively read:

$$C_d = \left(\frac{\kappa}{1 + \log\left(\frac{z_0}{h}\right)}\right)^2 \tag{C.4}$$

$$f_w = 1.39 \left(\frac{A_{orb}}{z_0}\right)^{-0.52} \tag{C.5}$$

where $\kappa \simeq 0.41$ is the von kármán constant and U_{orb}, A_{orb} are the local estimates of the orbital velocity and semi-orbital excursion at the bottom level at peak frequency:

$$U_{orb} = \frac{\pi}{\sqrt{2}} \frac{H_{m0}}{T_{pc} \sinh\left(kh\right)} \tag{C.6}$$

$$A_{orb} = \frac{U_{orb} T_{pc}}{2\pi} \tag{C.7}$$

The maximum skin friction velocity thus reads:

$$u^*_{max} = \sqrt{\frac{\tau_{max}}{\rho}} \tag{C.8}$$

Second, the settling velocity for the single class sediment was given by (Soulsby, 1997, Eq. 102):

$$W_s = \frac{\nu}{D} \left((10.36^2 + 1.049 D_*^3)^{1/2} - 10.36\right) \tag{C.9}$$

where $\nu \simeq 1.36 \cdot 10^{-6}\,\mathrm{m}^2/\mathrm{s}$ is the sea-water kinematic viscosity and D_* is the dimensionless grain size (see Soulsby, 1997, Eq. 98).

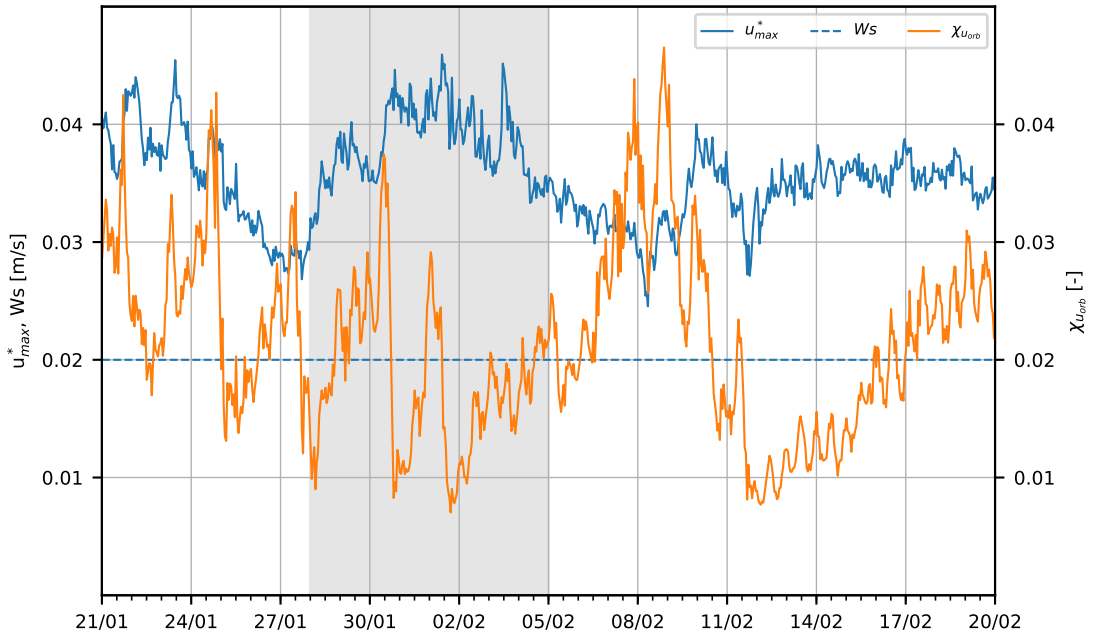

Figure 7: Skin friction velocity versus settling velocity of fine sand and relative short wave orbital velocities decrease between the wave cell and the OBS vertical locations.

References

Abdelrahman, S. and Thornton, E. (1987). Changes in the short wave amplitude and wavenumber due to the presence of infragravity waves. In *Coastal Hydrodynamics*, pages 458–478. ASCE.

Beach, R. A. and Sternberg, R. W. (1988). Suspended sediment transport in the surf zone: response to cross-shore infragravity motion. *Marine Geology*, 80(1-2):61–79.

Bertin, X., Castelle, B., Chaumillon, E., Butel, R., and Quique, R. (2008). Longshore transport estimation and inter-annual variability at a high-energy dissipative beach: St. trojan beach, sw oléron island, france. *Continental Shelf Research*, 28(10-11):1316–1332.

Bertin, X., Li, K., Roland, A., and Bidlot, J.-R. (2015). The contribution of short-waves in storm surges: Two case studies in the bay of biscay. *Continental Shelf Research*, 96:1–15.

Bertin, X., Martins, K., de Bakker, A., Chataigner, T., Guérin, T., Coulombier, T., and de Viron, O. (2020). Energy transfers and reflection of infragravity waves at a dissipative beach under storm waves. *Journal of Geophysical Research: Oceans*, 125(5):e2019JC015714.

Bishop, C. T. and Donelan, M. A. (1987). Measuring waves with pressure transducers. *Coastal Engineering*, 11(4):309 – 328.

Coulombier, T., Neumeier, U., and Bernatchez, P. (2012). Sediment transport in a cold climate salt marsh (st. lawrence estuary, canada), the importance of vegetation and waves. *Estuarine, Coastal and Shelf Science*, 101:64–75.

de Bakker, A., Brinkkemper, J., Van der Steen, F., Tissier, M., and Ruessink, B. (2016). Cross-shore sand transport by infragravity waves as a function of beach steepness. *Journal of Geophysical Research: Earth Surface*, 121(10):1786–1799.

Dibajnia, M. and Watanabe, A. (1992). Sheet flow under nonlinear waves and currents. *Coastal Engineering Proceedings*, (23).

Dodet, G., Bertin, X., Bouchette, F., Gravelle, M., Testut, L., and Wöppelmann, G. (2019). Characterization of sea-level variations along the metropolitan coasts of france: waves, tides, storm surges and long-term changes. *Journal of Coastal Research*, 88(sp1):10 – 24.

Dohmen-Janssen, C. M., Kroekenstoel, D. F., Hassan, W. N., and Ribberink, J. S. (2002). Phase lags in oscillatory sheet flow: experiments and bed load modelling. *Coastal Engineering*, 46(1):61–87.

Elgar, S., Gallagher, E. L., and Guza, R. (2001). Nearshore sandbar migration. *Journal of Geophysical Research: Oceans*, 106(C6):11623–11627.

Elgar, S. and Guza, R. T. (1985). Observations of bispectra of shoaling surface gravity waves. *Journal of Fluid Mechanics*, 161:425 – 448.

Grasso, F., Michallet, H., and Barthélemy, E. (2011). Sediment transport associated with morphological beach changes forced by irregular asymmetric, skewed waves. *Journal of Geophysical Research: Oceans*, 116(C3).

Guza, R., Thornton, E., and Holman, R. (1985). Swash on steep and shallow beaches. In *Coastal Engineering 1984*, pages 708–723.

Hamm, L. and Peronnard, C. (1997). Wave parameters in the nearshore: A clarification. *Coastal Engineering*, 32(2-3):119 – 135.

Hamon-Kerivel, K., Cooper, A., Jackson, D., Sedrati, M., and Pintado, E. G. (2020). Shoreface mesoscale morphodynamics: A review. *Earth-Science Reviews*, page 103330.

Hanes, D. M. and Huntley, D. A. (1986). Continuous measurements of suspended sand concentration in a wave dominated nearshore environment. *Continental Shelf Research*, 6(4):585–596.

Hsu, T.-J. and Hanes, D. M. (2004). Effects of wave shape on sheet flow sediment transport. *Journal of Geophysical Research: Oceans*, 109(C5).

Jaffe, B. E. and Rubin, D. M. (1996). Using nonlinear forecasting to learn the magnitude and phasing of time-varying sediment suspension in the surf zone. *Journal of Geophysical Research: Oceans*, 101(C6):14283–14296.

Jaffe, B. E., Sternberg, R. W., and Sallenger, A. H. (1985). The role of suspended sediment in shore-normal beach profile changes. In *Coastal Engineering 1984*, pages 1983–1996.

List, J. H. (1991). Wave groupiness variations in the nearshore. *Coastal Engineering*, 15(5-6):475–496.

Mouragues, A., Bonneton, P., Lannes, D., Castelle, B., and Marieu, V. (2019). Field data-based evaluation of methods for recovering surface wave elevation from pressure measurements. *Coastal Engineering*, 150:147 – 159.

Osborne, P. D. and Greenwood, B. (1992). Frequency dependent cross-shore suspended sediment transport. 1. a non-barred shoreface. *Marine Geology*, 106(1-2):1–24.

Pezerat, M., Bertin, X., Martins, K., and Lavaud, L. (2022). Cross-shore distribution of the wave-induced circulation over a dissipative beach under storm wave conditions. *Journal of Geophysical Research: Oceans*, 127(3):e2021JC018108.

Roelvink, J. and Stive, M. (1989). Bar-generating cross-shore flow mechanisms on a beach. *Journal of Geophysical Research: Oceans*, 94(C4):4785 – 4800.

Ruessink, B., Houwman, K., and Hoekstra, P. (1998). The systematic contribution of transporting mechanisms to the cross-shore sediment transport in water depths of 3 to 9 m. *Marine Geology*, 152(4):295–324.

Russell, P. E. (1993). Mechanisms for beach erosion during storms. *Continental Shelf Research*, 13(11):1243–1265.

Soulsby, R. (1997). *Dynamics of marine sands - A manual for practical applications*. Thomas Telford Publications, London.

Van Dongeren, A. R. and Svendsen, I. A. (1997). Quasi 3-d modeling of nearshore hydrodynamics. Research report, University of Delaware. CACR-97-04.